

# Journal of Materials Chemistry B

Accepted Manuscript



This is an *Accepted Manuscript*, which has been through the Royal Society of Chemistry peer review process and has been accepted for publication.

*Accepted Manuscripts* are published online shortly after acceptance, before technical editing, formatting and proof reading. Using this free service, authors can make their results available to the community, in citable form, before we publish the edited article. We will replace this *Accepted Manuscript* with the edited and formatted *Advance Article* as soon as it is available.

You can find more information about *Accepted Manuscripts* in the [Information for Authors](#).

Please note that technical editing may introduce minor changes to the text and/or graphics, which may alter content. The journal's standard [Terms & Conditions](#) and the [Ethical guidelines](#) still apply. In no event shall the Royal Society of Chemistry be held responsible for any errors or omissions in this *Accepted Manuscript* or any consequences arising from the use of any information it contains.

**Size-dependent toxicity and interactions of calcium oxalate dihydrate  
crystal on Vero renal epithelial cells**

Xin-Yuan Sun, Jian-Ming Ouyang\*, Wen-Yu Zhu, Yu-Bao Li, Qiong-Zhi Gan

(Department of Chemistry, Jinan University, Guangzhou 510632, China; Institute of  
Biomineralization and Lithiasis Research, Jinan University, Guangzhou 510632, China)

---

Corresponding authors. *E-mail address:* [toyjm@jnu.edu.cn](mailto:toyjm@jnu.edu.cn)

**Abstract: Objective:** Urinary crystals in normal and kidney stone patients often have varying sizes, the interaction between renal epithelial cells and COD crystals generated in the tubular fluid could play an initiating role in the pathophysiology of calcium oxalate nephrolithiasis. This study aims to compare the cytotoxicity of micro/nano-calcium oxalate dihydrate (COD) crystals (50 nm, 100 nm, 600 nm, 3  $\mu\text{m}$ , and 10  $\mu\text{m}$ ) toward African green monkey renal epithelial (Vero) cells to reveal the mechanism of kidney stone formation at the molecular and cellular levels. **Methods:** Vero cells were exposed to COD crystals of varying sizes at a concentration of 200  $\mu\text{g/mL}$  for 6 h. The effects of COD crystals on Vero cell viability, apoptosis rate, and cellular biochemical parameters [(lactate dehydrogenase (LDH), superoxide dismutase (SOD), reactive oxygen species (ROS), hyaluronic acid (HA), osteopontin (OPN), and mitochondrial membrane potential ( $\Delta\psi/\text{m}$ )] were determined using biochemical and morphological analyses. **Results:** Vero cell viability and apoptotic rate were closely associated with the size of COD crystals; lower cell viability and higher apoptosis rate was observed in cells exposed to smaller COD crystal size. The expression of SOD, ROS, HA and OPN also changed in a size-dependent manner after exposure to the five different sizes of COD crystals. The area ratio of the (100) face with a high density of  $\text{Ca}^{2+}$  ions to total surface area was also found to influence the severity of cell injury. Cell injury induced by COD crystals was mainly caused by excessive expression of intracellular ROS and reduction of free-radical scavenger SOD. Moreover, binding of large crystals on the cell membrane surface takes more time to cause cell injury than internalized small-sized crystals. Cell death rate was found to be positively correlated with the amount of internalized COD crystals. **Conclusions:** Although COD toxicity is often disregarded, the size-dependent cytotoxicity of COD crystals toward Vero cells was demonstrated in this study.

**Keywords:** Size-dependent toxicity; Micro/nano crystals; Calcium oxalate; Oxidative damage; Adhesion and internalization; Biomineralization

## 1. Introduction

Urolithiasis is a frequently occurring disease, its main component is calcium oxalate (CaOx). The formation of CaOx stones is a complex biological control process that includes crystal nucleation, growth, aggregation, and retention of crystals in vivo [1,2]. In general, the transient time of urine microcrystallines across the kidney is too short for crystals to grow large enough to block the urinary tract [3]. Crystal retention is mainly caused by the adhesion of crystals on renal tubular epithelial cells [4]. Thus, renal tubular epithelial cell injury is an important factor in the formation of CaOx stones [5,6].

CaOx stones mainly contain two components: calcium oxalate monohydrate (COM) and dehydrate (COD). COM crystals have been extensively studied for their capacity to induce cell injury [7–9]. COD is the secondary common type of kidney stone and the most frequent calcium oxalate crystal present in the urine of patients with idiopathic calcium urolithiasis [10]. Unfortunately, limited studies have been conducted regarding the effect of COD crystals on renal epithelial cells; in addition, only micron-graded COD crystals have been used for these studies [11,12].

The interaction between exogenous materials and biological system has gained increasing attention [13–15]. Size, which is an important physical parameter for crystals, plays a vital role in the interaction between micro/nano particles and cells. For instance, compared with 3  $\mu\text{m}$  CuO particles, 42 nm nano-CuO particles exhibit higher cytotoxicity and cause cell death, mitochondrial damage, DNA damage, and oxidative DNA lesions of the human cell line A549 [16]. Yang et al. [17] reported that amorphous nano-SiO<sub>2</sub> exposure induces more severe cytotoxicity in HaCaT cells than micro-sized SiO<sub>2</sub> particles, with the expression levels of the differentially expressed proteins associated with the particle size.

Urinary crystals in normal and kidney stone patients often have different sizes, crystal phases, and morphologies because of differences in the supersaturation of lithogenic salts, pH value, viscosity, and retention time of microcrystalline among individuals [18–23]. Robertson et al. [21] found that recurrent stone formers excrete more crystalline calcium oxalate than their controls under similar conditions of diet and fluid intake; the difference is mainly due to increasing crystal size rather than increasing crystal number; the calcium oxalate crystalluria in recurrent stone formers mainly comprises octahedral COD crystals with 10–12  $\mu\text{m}$  diameter and often are fused into polycrystalline aggregates with 20–300  $\mu\text{m}$  diameter. In the controls, calcium oxalate is in the form of very small particles with 3–4  $\mu\text{m}$  diameter with few or no aggregation. In our early study [22], the nanocrystallites with a size of less than 1,000 nm in the urine samples of 85 healthy persons and 65 lithogenic patients were comparatively investigated. Most of the nanocrystallites in healthy urine samples were with a narrow particle size distribution from about 20 nm to 400 nm. In contrast, most of the particles in lithogenic urines had a broad particle size distribution from 1.1 nm to 1,000 nm.

However, the impact of different crystal properties toward renal epithelial cells is still not clear, especially the differences between nanocrystalline and microcrystalline known at present in urine have not been reported.

Based on these reasons, five COD crystals of varying sizes (from 50 nm to 10  $\mu\text{m}$ ) were prepared and comparatively studied for their cytotoxicity toward African green monkey renal epithelial (Vero) cells to reveal the mechanism of kidney stone formation at the molecular and cellular levels.

## **2. Materials and methods**

### **2.1 Materials and Apparatus**

(1) Materials: African green monkey renal epithelial (Vero) cells were purchased from Shanghai

Cell Bank, Chinese Academy of Sciences (Shanghai, China). DMEM culture medium was purchased from HyClone Biochemical Products Co., Ltd. (UT, USA). Fetal bovine serum was purchased from Hangzhou Sijiqing Biological Engineering Materials Co., Ltd. (Hangzhou, China). Penicillin and streptomycin were purchased from Beijing Pubo Biotechnology Co., Ltd. (Beijing, China). Cell culture plates were purchased from Wuxi Nest Bio-Tech Co., Ltd. (Wuxi, China).

Cell proliferation assay kit (CCK-8) was purchased from Dojindo Laboratories (Kumamoto, Japan). Lactate dehydrogenase (LDH) kit, biotinylated hyaluronic acid binding protein (bHABP) (MERCK Corporation, Germany), propidium iodide (PI), 4,6-diamidino-2-phenylindole (DAPI) staining solution, anti-fade fluorescence mounting medium and bovine serum albumin (BSA) were all purchased from Shanghai Beyotime Bio-Tech Co., Ltd. (Shanghai, China). Fluorescein FITC-Avidin was purchased from Wuhan Boster Biological Engineering Co., Ltd. (Wuhan, China).

All conventional reagents used were analytically pure and purchased from Guangzhou Chemical Reagent Factory of China (Guangzhou, China).

(2) Apparatus: The apparatus used include X-L type environmental scanning electron microscope (SEM, Philips, Eindhoven, Netherlands), laser confocal microscope (LSM510 Meta Duo Scan, Zeiss, Jena, Germany), inverted fluorescence microscope (IX51, Olympus, Tokyo, Japan), enzyme mark instrument (Safire2™, Tecan, Männedorf, Switzerland), inductively coupled plasma emission spectrometer (ICP-AES, Optima 2000DV, Perkin Elmer, CT, USA) and flow cytometer (FACS Aria, BD Corporation, CA, USA).

## **2.2 Experimental methods**

### **2.2.1 Preparation of different-sized COD crystals and COD crystal suspension**

Five COD crystals with different sizes (50 nm, 100 nm, 600 nm, 3 μm, and 10 μm) were prepared as previously described [24,25] by changing the concentration of reactants, reaction

temperature, solvent, mixing manner, and stirring speed. A buffer solution was also used to control the pH of the solution. Crystal growth inhibitors were not added into the reaction system during crystal preparation. A combination of SEM, XRD, and FT-IR results revealed that all prepared COD crystals were the pure target product. The details would be reported elsewhere.

For the preparation of different-sized COD crystal suspension, a certain amount of COD crystals were UV sterilized for 40 min and dispersed in serum-free DMEM culture medium at a concentration of 200  $\mu\text{g}/\text{mL}$ .

### 2.2.2 Cell culture

Vero cells were cultured in DMEM culture medium containing 10% fetal bovine serum in a 5%  $\text{CO}_2$  humidified atmosphere at 37  $^\circ\text{C}$ . Trypsin digestion method was adopted for cell propagation. Upon reaching 80%–90% confluence, the cells were rinsed twice with PBS. A certain amount of 0.25% trypsin digestion solution was then added and maintained for 3–5 min at 37  $^\circ\text{C}$ . Afterward, DMEM containing 10% fetal bovine serum was added to terminate the digestion. The cells were then blown well to form single cell suspensions.

### 2.2.3 Cell viability assay

One hundred microliters of cell suspension with a cell concentration of  $1 \times 10^5$  cells/mL was inoculated per well in 96-well plates and incubated for 24 h. Afterward, the medium was changed to serum-free culture media and then incubated for another 12 h to achieve synchronization. The culture medium was removed by suction and the cells were washed twice with PBS. The experimental model was divided into two groups: (A) control group, in which only serum-free culture medium was added; (B) treatment group with COD crystals, in which cells were exposed to five sizes of COD crystals (50 nm, 100 nm, 600 nm, 3  $\mu\text{m}$ , and 10  $\mu\text{m}$ ) at a concentration of 200  $\mu\text{g}/\text{mL}$  prepared with serum-free culture medium, respectively. Each experiment was repeated in

three parallel wells. After incubation for 6 h, 10  $\mu$ l CCK-8 was added to each well and incubated for 1.5 h. Absorbance (A) was measured by using the enzyme mark instrument at 450 nm. Cell viability was determined using the equation below.

$$\text{Cell viability (\%)} = \frac{A(\text{treatment group})}{A(\text{control group})} \times 100 \%$$

#### 2.2.4 Lactate dehydrogenase (LDH) release assay

One hundred microliters of cell suspension with a cell concentration of  $1 \times 10^5$  cell/mL was inoculated per well and incubated for 24 h. Afterward, the medium was changed to serum-free culture media and then incubated for another 12 h to achieve synchronization. The experimental model was divided into four groups: (A) cell-free culture medium wells (control wells of background); (B) control wells without drug treatment (sample control wells); (C) cells without drug treatment for the subsequent cleavage of the wells (sample maximum enzyme activity control wells); and (D) treated group with different sizes of COD at a concentration of 200  $\mu$ g/mL (drug-treated wells). After incubation, the absorbances were analyzed at 490 nm according to the LDH kit instruction.

$$\text{LDH\%} = \frac{A(\text{Group D}) - A(\text{Group A})}{A(\text{Group C}) - A(\text{Group A})} \times 100\%$$

#### 2.2.5 Intracellular superoxide dismutase (SOD) assay

One hundred microliters of cell suspension with a cell concentration of  $1 \times 10^5$  cell/mL was inoculated per well in 96-well plates and incubated for 24 h. Afterward, the medium was changed to serum-free culture media and then incubated for 12 h to achieve synchronization. The cells were exposed to COD crystals of varying sizes at a concentration of 200  $\mu$ g/mL for 6 h. Then, the liquid supernatant was collected to measure the SOD activity according to the SOD kit instructions.

#### 2.2.6 Intracellular ROS assay

Two milliliters of cell suspension with a cell concentration of  $1 \times 10^5$  cells/mL was inoculated

per well in six-well plates. After synchronization, the cells were grouped. COD crystals of varying sizes were then added. After 6 h incubation, the supernatant was aspirated and the cells were washed twice with PBS and digested with 0.25% trypsin. Afterward, DMEM supplemented with 10% fetal bovine serum was added to terminate digestion. The cells were suspended by pipetting, followed by centrifugation (1000 rpm, 5 min). The supernatant was aspirated and the cells were washed once with PBS and centrifuged again to obtain a cell pellet. The cells were resuspended by adding and thoroughly mixing 500  $\mu$ L of PBS in a microcentrifuge tube. The samples were then stained with 2', 7'-dichloro-fluorescein diacetate (DCFH-DA) and analyzed.

### 2.2.7 HA expression assay

One milliliter of cell suspension with a cell concentration of  $1 \times 10^5$  cells/mL was inoculated per well in 12-well plates. After synchronization, the cells were grouped. COD crystals of varying sizes were then added. After 6 h incubation, the supernatant was aspirated and the cells were washed twice with PBS. Afterward, the cell were fixed with fixation fluid (composed of 5% glacial acetic acid, 10% formalin, and 70% ethyl alcohol) and washed three times. One hundred microliters of 5  $\mu$ g/mL bHABP solution (prepared in 3% bovine serum albumin solution, fresh prepared) was then added to the cells and incubated at 4 °C overnight. Afterward, the cells were washed with PBS three times for 5 min each. One hundred microliters of FITC-avidin (fluorescein isothiocyanate-avidin) was added to the cells and incubated for 1 h. The cells were washed with PBS three times for 5 min each. DAPI staining solution was then added to the cells and incubated for 4 min. The cells were again washed with PBS three times for 5 min each. Finally, the prepared samples were mounted with anti-fade fluorescence mounting medium and observed in a confocal microscope. HA expression and cell nuclei were stained green and blue, respectively.

Quantitative analysis: HA fluorescence intensity was analyzed by Axiovision software (ZEISS, Jena, Germany). HA expressions in 100 cells were quantitatively detected for each group.

### 2.2.8 Osteopontin (OPN) expression assay

One thousand microliters of cell suspension with a cell concentration of  $1 \times 10^5$  cell/mL was

inoculated per well in 12-well plates and incubated until confluent monolayers formed. Afterward, the culture media were discarded and the cells were rinsed with D-Hanks and then incubated in serum-free culture media with COD crystals of varying sizes for 6 h. The supernatant was aspirated and the cells were washed with PBS three times for 5 min each. The cells were then fixed with 4% paraformaldehyde for 10 min. Afterward, the cells were washed with PBS three times for 3 min each. The cells were incubated in sheep serum for 20 min. Afterward, the first OPN antibody (1:100) (CA, USA) was mixed into the samples and incubated at 4 °C overnight. The cells were then washed with PBS three times for 5 min each. Afterward, FITC secondary antibody (1:100) (CA, USA) was added to the cells in the dark and incubated at 37 °C for 0.5 h. The cells were again washed with PBS three times for 5 min each. Finally, the cells were stained and sealed with DAPI. Fluorescence was observed using a laser confocal fluorescence microscope. OPN expression and cell nuclei were stained green and blue, respectively.

### **2.2.9 Measurement of mitochondrial membrane potential ( $\Delta\psi_m$ )**

The density of seeded cells and experimental grouping were the same as those in Section 2.2.6. After 6 h of incubation, the supernatant was aspirated and the cells were washed twice with PBS and digested with 0.25% trypsin. DMEM supplemented with 10% fetal bovine serum was then added to terminate digestion. The cells were suspended by pipetting, followed by centrifugation (1000 rpm, 5 min). The supernatant was aspirated and the cells were washed with PBS and centrifuged again to obtain a cell pellet. The cells were resuspended by adding and thoroughly mixing 500  $\mu$ l of PBS in a microcentrifuge tube. Finally, the samples were stained with 5,5',6,6'-tetrachloro-1,1',3,3'-tetraethyl-imidacarbocyanine iodide (JC-1) and then analyzed.

### **2.2.10 Cellular apoptosis assay**

Apoptosis induced by varying sizes of COD crystals in Vero cells was measured by FCM with Annexin V-FITC/PI double staining assay. Briefly, the cells were harvested after 6 h of exposure to 200  $\mu$ g/mL of COD crystals, and then stained using Annexin V-FITC/PI apoptosis assay kit

according to the manufacturer's instructions. About  $1.5 \times 10^5$  cells were collected and washed with PBS (centrifuged at 1000 rpm for 5 min). The cells were resuspended in 200  $\mu$ L binding buffer. Afterward, 5  $\mu$ L Annexin V-FITC was added and then incubated in darkness at room temperature for 10 min. The cells were again resuspended in 200  $\mu$ L binding buffer and stained with 5  $\mu$ L PI. The prepared cells were then analyzed using a flow cytometer.

### **2.2.11 SEM observation of adhered COD crystals on Vero cell surface**

The density of seeded cells and experimental grouping were the same as those detected by HA. After reaching the adhesion time, the supernatant was removed by suction, washed three times with PBS, fixed in 2.5% glutaraldehyde at 4 °C for 24 h, fixed with 1% OsO<sub>4</sub>, washed three times with PBS, dehydrated in gradient ethanol (30%, 50%, 70%, 90% and 100%, respectively), dried under the critical point of CO<sub>2</sub>, and treated with gold sputtering. The crystal adhesion was observed by SEM.

### **2.2.12 Quantitative analysis of COD internalization by ICP-AES**

One milliliter of cell suspension with a cell concentration of  $1 \times 10^5$  cells/mL was inoculated per well in 12-well plates and incubated for 12h. After synchronization, the cells were grouped. COD crystals of varying sizes were then added. After 6 h incubation, the supernatant was aspirated and the cells were washed three times with PBS to remove unbound COD and then treated with 0.4 mL EDTA (4 mM) for 8 min to remove the bound COD. After the EDTA treatment, the cells were rinsed three times with cold PBS to completely remove the external soluble COD. The samples were then transferred to 25 mL beakers and mixed with 4.0 mL concentrated HNO<sub>3</sub> and 1.0 mL HClO<sub>4</sub> solution for digestion. A separate HClO<sub>4</sub> solution was heated until smoke appeared; the heat was then used to dry the solution. After cooling, 3 mL of 2% dilute HNO<sub>3</sub> was added. An inductively coupled plasma emission spectrometer (ICP-AES) was used to measure the concentration of Ca<sup>2+</sup> ions, which was then converted to determine the amount of COD internalization. The control group was treated using the same method to determine the interference of intracellular Ca<sup>2+</sup> in Vero cells.

### 2.2.13 Statistical analysis

The experimental results were analyzed statistically using SPSS 13.0 software and expressed as mean $\pm$ SE from three independent experiment.

## 3. Results

### 3.1 Characterization of COD crystals by SEM

The SEM images of the prepared COD crystals of varying sizes are shown in Fig. 1. The mean sizes of the crystals are as follows:  $50 \pm 10$  nm,  $100 \pm 20$  nm,  $600 \pm 100$  nm,  $3 \pm 1$   $\mu$ m, and  $10 \pm 2$   $\mu$ m, respectively.

Morphological changes were also observed together with the change in size of the COD crystal: 50 nm COD crystals are mainly spherical. Some part of the 600 nm crystals assume thick tetragonal bipyramid structures. All of the 10  $\mu$ m crystals assume thin tetragonal bipyramid structures. The schematic representation of morphology and crystal face variation of different sizes of COD crystals is presented in Fig. 2. The differences in the crystal faces of COD crystals are related to the rule of natural crystal growth. Classical crystallization theory indicates that the diverse crystal morphologies of similar minerals are due to the differences in the crystal faces with regard to surface energy and external growth environment [26]. Generally, the growth rate of a crystal face is related to its surface energy if a similar growth mechanism functions on each face [26,27]. Fast-growing faces exhibit high surface energies that disappear in the final morphology, and vice versa.

Considering the changes in the crystal faces of the three large-sized COD crystals (600 nm, 3  $\mu$ m, and 10  $\mu$ m) (Figs. 1 and 2), we could infer that the (100) face exhibits higher surface energy than the (101) face because of its faster growth rate. Hence, small COD crystals demonstrate large (100) face area and large-sized COD crystals present relatively small (100) face area. That is, the (100) and (101) faces disproportionately change with increasing crystal size. In addition, the ratio of

the (100) face area to the (101) face area ( $A_{(100)}/A_{(101)}$ ) gradually decreases with increasing crystal sizes as can be observed in submicron- and micron-sized COD crystals with regular structures.

### 3.2 Effects of COD crystal size on cell viability, LDH release, and SOD activity

The viability of Vero cells after exposure to varying sizes of COD crystals for 6 h was detected by CCK-8 assay (Fig.3a). Under the same concentration (200  $\mu\text{g}/\text{mL}$ ), cell viability increased from 66.7% to 88.5% as the crystal size increased from 50 nm to 10  $\mu\text{m}$ . The cell viability was found to be closely associated with crystal size. Cell injury induced by COD crystals was found to be size-dependent and followed the order 50 nm > 100 nm > 600 nm > 3  $\mu\text{m}$  > 10  $\mu\text{m}$  > control group; that is, the smaller the COD crystal size, the higher its cytotoxicity.

LDH is a stable enzyme of the cytoplasm that is released extracellularly once the cell membrane ruptures. Thus, LDH is considered as a marker of cell membrane integrity [28]. As shown in Fig. 3b, all five COD crystals could cause increase in LDH release (9.76%–5.08%). In addition, the amount of LDH released was found to be size-dependent and followed the order 50 nm > 100 nm > 600 nm > 3  $\mu\text{m}$  > 10  $\mu\text{m}$  > control group.

Decrease in SOD activity indicates that the ability of an organism to resist free radical injury is weakened, and the degree of free radical injury to the organism is enhanced. As shown in Fig. 3c, SOD activity in all five crystal-treated groups decreased, with the same regularity as that of cell viability; that is, the smaller the COD crystal size, the greater the decrease in SOD activity.

### 3.3 Intracellular ROS generation induced by varying sizes of COD crystals

ROS levels, which can be elevated by pathological and physiological stimuli, indicate the degree of oxidative stress inside the cell. Oxidative stress occurs when the generation of ROS overwhelms the natural antioxidant defenses of cells. Renal cellular exposure to oxalate (Ox) and/or CaOx crystals could lead to the production of ROS, development of oxidative stress, followed by

injury and inflammation [29].

To further elucidate the mechanisms of COD cytotoxicity, intracellular ROS levels of the different treatment groups were determined (Fig. 4). The intracellular ROS level of Vero cells after exposure to varying sizes of COD crystals elevated in a size-dependent manner; that is, the smaller the COD crystal size, the more intracellular ROS generated.

### **3.4 HA release induced by varying sizes of COD crystals**

HA is an important crystal-binding molecule that is upregulated during various inflammatory disease states [30]. HA expression in Vero induced by varying sizes of COD was detected by laser confocal microscopy (Fig. 5). Compared with normal cells with weak green fluorescence, Vero cells treated with 50 nm COD crystals emitted the strongest green fluorescence. Based on quantitative analysis, HA expression in the COD crystal-treated cells was found to be size dependent and followed the order 50 nm > 100 nm > 600 nm > 3  $\mu$ m > 10  $\mu$ m > control group; that is, the smaller COD induces more severe cell injury and greater HA expression.

### **3.5 OPN expression induced by varying sizes of COD crystals**

OPN is widely spread throughout organs and tissues, including the kidney. In healthy kidney, OPN is confined to the distal parts of a subset of nephrons and would be obviously upregulated after renal epithelial cell injury [31]. OPN expression in Vero cells after treatment with varying sizes of COD crystals is shown in Fig. 6. Compared to the control group where minimal OPN expression was observed, all the crystal-treated groups showed obvious green fluorescence. The fluorescence intensity of nano groups (50 and 100 nm) was obviously higher than that in the micro groups, indicating that smaller crystals induce higher OPN expression.

### 3.6 Decrease in mitochondrial membrane potential caused by COD and time effect

Decrease in mitochondrial membrane potential ( $\Delta\psi_m$ ) is a representative event in early apoptosis. JC-1 differentially labels mitochondria with high and low  $\Delta\psi_m$  by forming J-aggregates or monomers that emit orange-red or green light, respectively [32].

We analyzed the changes in  $\Delta\psi_m$  in cells treated with varying sizes of COD crystals using a mitochondrial membrane potential assay kit. Compared with the control group, all five sizes of COD caused  $\Delta\psi_m$  to decrease. The three smaller COD crystals (50, 100, and 600 nm) caused the greater  $\Delta\psi_m$  decrease compared with 3  $\mu\text{m}$  and 10  $\mu\text{m}$  COD (Figs. 7A and 7B).

Moreover, two representative COD crystals were selected (a nano-crystal and a micro-crystal) and assessed for their effect in  $\Delta\psi_m$  under different time treatments (Fig. 7C). The result show that 50 nm COD caused an obvious decrease (about 16.1%) in  $\Delta\psi_m$  as early as 3 h treatment time, whereas 10  $\mu\text{m}$  COD caused only 1.8% decrease in  $\Delta\psi_m$ . However, when treatment time was increased to 12 h, 10  $\mu\text{m}$  COD also caused a significant decrease in  $\Delta\psi_m$  (9.4%).

### 3.7 Apoptosis of Vero cells induced by varying sizes of COD crystals

Flow cytometric analysis show that varying sizes of COD crystals induced apoptosis in a size-dependent manner (Fig. 8). The apoptosis rates of the five treated groups were all higher than that of the control group, of which 50 nm COD crystals induced the highest apoptosis rate. The apoptosis rate of the 50 nm, 100 nm, 600 nm, 3  $\mu\text{m}$  and 10  $\mu\text{m}$  COD-treated groups were 14.5%, 11.4%, 8.4%, 4.7%, and 2.4%, respectively. Under the same concentration of 200  $\mu\text{g}/\text{mL}$ , the effects of micro-sized COD crystals on cell apoptosis were much milder than that of nano-sized COD crystals, indicating that nanoparticles had stronger cytotoxicity than microparticles.

### 3.8 SEM detection of adhesion between Vero and varying sizes of COD crystals

The SEM images of Vero cells after exposure to varying sizes of COD for 6 h are presented in Fig. 9. The following observations can be noted:

1) Small COD crystals aggregated on the cell surface at a greater extent compared to large COD crystals. For instance, the nano-sized COD crystals (50 and 100 nm) exhibited obvious aggregation after adhering to Vero cells. By contrast, slight aggregation was observed in 600 nm COD crystals, which was more minimal in the larger 3 and 10  $\mu\text{m}$  COD crystals.

2) The number of crystals that adhered on the cell surface decreased with increasing COD crystal size.

For the 10  $\mu\text{m}$  COD crystals, only a small part of the cells was in contact with COD crystals. The number of crystals was less than that of the cells, so two types of cells may be observed.

The first type comprises cells that are in contact with large COD crystals (Figs. 9e, 10a and 10b). These cells that were injured by crystal adhesion significantly shrank to about 10  $\mu\text{m}$ . They have rough surfaces and contain small particles owing to protein, lipid, and sugar secretions.

The second type are cells that have no crystals on their surfaces (Figs. 10c and 10d). These cells have smooth surfaces similar to that of normal cells, and are spindle-shaped with length of about 20–25  $\mu\text{m}$ , indicating a smaller degree of injury.

As shown in Table 1, under the same concentration of 200  $\mu\text{g/mL}$ , the number of crystals decreased significantly with increasing COD crystal size. For the 10  $\mu\text{m}$  COD crystal group, every six cells could be in contact with only one crystal. Most cells had no chance to be in contact with COD crystals (Fig. 10), and hence, had minimal injury. Therefore, the injury induced by 10  $\mu\text{m}$  COD crystals was much weaker than that caused by the smaller COD crystals.

3) Compared to the high adhesion ability of micro-COM to cells, the adhesion ability of micro-COD toward cells is much milder [33]. However, long treatment (6 h) exposure to high concentration of micro-COD suspension could also cause cell injury (Figs. 3–10).

### 3.9 Quantitative analysis of COD internalization by Vero cells

For the quantitative analysis of COD internalized by Vero cells, 4 mM EDTA was used to remove externally bound COD crystals [34]. The uptake of COD into the cell was then measured by ICP-AES. The result shows that internalization is closely related to COD crystal size (Fig. 11). Among the five groups, 50 nm COD crystals exhibited the highest internalization ( $16.3 \mu\text{g}/\text{cm}^2$ ). The amount of internalized crystals was found to decrease with increasing crystal size; 10  $\mu\text{m}$  COD crystals were hardly internalized because of their large size.

From the correlation analysis, cell death rate was found to be positively related to the amount of internalized crystals ( $R^2 = 0.9444$ ).

## 4. Discussion

Urinary supersaturation is the driving force behind crystal formation in the kidneys, and it is closely related to the size of the initial formed crystallites. Mersmann et al. [35] stated that the median crystal size is affected by the mean relative supersaturation for inorganic and organic systems, and the median crystal size drops with increasing relative supersaturation. In fact, stone formers tend to excrete urine that is more supersaturated than that of non-stone formers [36]. Thus, the initial formed urine crystallites in stone-formers would be smaller than that in healthy controls, but the excreted crystallites in urine were not any more the initial formed crystallites which have undergone a series of physicochemical changes containing crystal growth and aggregation [2, 37]. So far, the impact of crystal size toward renal epithelial cell injury has not yet attracted much concern.

### 4.1 Size-dependent toxicity of COD crystals on Vero cells

Under the same crystal concentration of 200  $\mu\text{g}/\text{mL}$ , cell injury and toxicity of varying sizes of COD crystals to Vero cells was found to be size-dependent (Figs.3–10): 50 nm > 100 nm > 600 nm >

3  $\mu\text{m}$  > 10  $\mu\text{m}$ . The possible reasons for this difference are discussed below:

### 1) Small-size effect of nano-COD crystals

The higher injury ability of nano-COD crystals toward cells, which is obviously higher than traditional micro-crystals, may be attributed to the smaller crystal size. As shown in Fig. 4, intracellular ROS content gradually increased with decreasing COD size from 10  $\mu\text{m}$  to 50 nm. Excessive ROS generation could induce oxidative stress, which is a key mechanism for nanoparticle toxicity [38].

Owing to the high surface area of small COD crystals, more active sites are created to capture oxygen molecules, which leads to the production of superoxide radical ( $\bullet\text{O}_2^-$ ) and other ROS through dismutation or Fenton reaction [39]. Excessive formation of cellular ROS could induce mitochondrial membrane permeability, ultrastructural mitochondrial damage, and disruption of the respiratory chain to trigger apoptosis [40]. Therefore, cell apoptosis induced by small COD crystals is more serious than that of large-sized crystals.

Although the differences in cell injury induced by varying sizes of COD crystals have not been reported, the effect of size in other materials has been studied extensively. For instance, 20–80 nm nano-calcium phosphates could significantly inhibit the proliferation of osteosarcoma U2OS cells, whereas ordinary rod-like calcium phosphates (length: 300–500 nm, diameter: 30–80 nm) have no inhibitory effect [41]. Li et al. studied the potential cytotoxicity of amorphous silica particles with different sizes (498, 68, 43, and 19 nm) in cultured human hepatoma (HepG2) cells; the cytotoxicity generated by silica particles strongly depended on particle size; smaller silica particle possessed higher toxic effect and induced decrease in cell number, cellular shrinkage, chromatin condensation, and vacuolar degeneration [42]. In addition, smaller  $\text{SiO}_2$  was found to induce more multinucleated cells, which rarely occurred in the Si498-treated group and the control group.

### 2) More positive charges on the surface of small-sized COD crystals enhance their

### interaction with Vero cells

COD crystals usually possess tetragonal bipyramid structure consisting of four symmetry-related (100) face and eight (101) face (constituting the two vertices). With increasing COD crystal size, the morphology of COD crystals gradually changes from a small-sized sphere ( $\leq 100$  nm) to a thick medium-sized tetragonal bipyramid (600 nm), and eventually, to a thin large-sized tetragonal bipyramid ( $\geq 3$   $\mu\text{m}$ ) (Fig. 2). The (101) face area ( $A_{(101)}$ ) increased and the (100) face area ( $A_{(100)}$ ) relatively decreased with increasing crystal sizes as can be observed in submicron- and micron-sized COD crystals with regular structures, leading to a decrease in  $A_{(100)}/A_{(101)}$  ratio. Hence, besides the size effect of varying sizes of COD on cytotoxicity, the variation of crystal face area was also related to their toxicity on Vero cells.

The surface concentrations of  $\text{Ca}^{2+}$  ions in the (100) face ( $0.0439 \text{ Ca}^{2+}/\text{A}^2$ ) of COD was obviously higher than that of the (101) face ( $0.0225 \text{ Ca}^{2+}/\text{A}^2$ ) [33], the adhesion force of the (100) face with more positive charges was higher than that of the (101) face. AFM detection also showed that the adhesion force between the (100) face of COD crystal and AFM tips modified with  $\text{S}(\text{CH}_2)_{10}\text{COO}^-$  or  $\text{S}(\text{CH}_2)_2\text{NHC}(\text{NH}_2^+)\text{NH}_2$  was obviously higher than that of the (101) face. Therefore, the (100) face of COD crystals preferentially adheres to the plasma membrane of renal cells [43]. At the same time, the  $\text{Ca}^{2+}$  ion-rich (100) face theoretically induces more obvious phosphatidylserine eversion and cell depolarization [44], thus causing more severe cell injury.

Consequently, 50 nm COD crystals induced maximum toxicity toward Vero cells, leading to the observed decrease in cell viability, SOD activity, and  $\Delta\psi\text{m}$  (Figs. 3a, 3c, and 7); increase in LDH release, intracellular ROS level, and apoptosis rate (Figs. 3b, 4, and 8); and increased expression of adhesion molecules such as HA (Fig. 5) and OPN (Fig. 6). By contrast, 10  $\mu\text{m}$  COD crystals caused the weakest injury toward Vero cells.

### 3) The smaller the COD size, the higher the crystal adhesion and the larger the injury on

**cells**

Under the same concentration, smaller crystals occur in greater number (Table 1), which increases their injury probability toward cells. Therefore, the injury to Vero cells is significantly enhanced in nano-COD crystals. Analysis of the contact probability between Vero cells and varying sizes of COD crystals under fixed crystal concentration (200  $\mu\text{g/mL}$ ) showed that the number of crystals and contact probability decreased with increasing COD crystal size. For the 10  $\mu\text{m}$  COD-treated group, about every six cells could be in contact with only one crystal. Most of the cells had no chance to be in contact with crystals (Fig. 10), and hence, had minimal injury. By contrast, every cell can be assigned to  $1.29 \times 10^6$  crystals for the 50 nm COD-treated group. Therefore, the 10  $\mu\text{m}$  COD crystals induced the weakest injury toward Vero cells.

**4) Difference in internalization of varying sizes of COD crystals in Vero cells**

A high correlation was found between the amount of internalized exogenous particles and cytotoxicity [34]. Smaller COD crystals ( $\leq 600$  nm) were easily internalized by the cells (Fig. 11) [45]. The increased LDH release also indicates that cell membrane fluidity improved, which further promoted cell endocytosis of COD crystals (Fig. 3b). By contrast, large COD crystals (3–10  $\mu\text{m}$ ) were difficult to uptake into the cells. Therefore, the injury induced by nano-COD crystals was greater than that of micro COD crystals. Many studies also reported that cellular uptake of exogenous materials is closely related with crystal size [46,47].

With increasing treatment time,  $\Delta\psi\text{m}$  in 10  $\mu\text{m}$  COD-treated group obviously decreased (Fig. 7c). However, based on ICP results, Vero cells could hardly uptake the large crystals (Fig. 11a). This finding implies that it takes more time to cause cell injury by large crystals binding on cell membrane surface than that of internalized small crystals. In addition, the degree of injury in large crystal-treated groups was much less than that in small crystal-treated groups (Fig. 7c).

A direct correlation was found between the amount of internalized exogenous particles and cell

injury. Based on the correlation (Fig. 11b), cell death rate was positively related to the amount of internalized crystals. Such result suggested that the internalized COD crystals may be the primary cause of Vero cell death.

#### 4.2 Injury mechanism of Vero cells induced by varying sizes of COD crystals

Based on the above results, a model of Vero cell injury mechanism induced by varying sizes of COD crystals is proposed (Fig. 12).

Interaction of varying sizes of COD crystals with Vero cells upregulates NADPH oxidase and stimulates the generation of  $\bullet\text{O}_2^-$  via NADPH oxidase [48]. Excessive  $\bullet\text{O}_2^-$  formation could induce mitochondrial dysfunction, which further causes the formation of  $\bullet\text{O}_2^-$  and, eventually, oxidative stress (Fig. 4). At the same time, intracellular  $\bullet\text{O}_2^-$  could be converted into  $\text{H}_2\text{O}_2$  with SOD, which results in the observed decline in the amount of SOD (Fig. 3c). However, excessive  $\bullet\text{O}_2^-$  formation could overwhelm the natural scavenging activity of cells, which causes  $\Delta\psi_m$  decrease (Fig. 7) and even apoptosis (Fig. 8). This phenomenon leads to the increase in LDH release (Fig. 3b), phosphatidylserine (PS) eversion [49], HA expression (Fig. 5), and OPN upregulation (Fig. 6). Moreover, COD crystals could combine with negatively charged molecules and aggravate their adhesion and internalization toward Vero cells.

Compared to large COD crystals, small COD crystals possess higher specific surface area, and hence, more exposed active sites and higher ratio of  $\text{Ca}^{2+}$  ion-rich (100) face area to total surface area. The interaction between small COD crystals and Vero cells is greater than that in large COD crystals. Therefore, the toxicity induced by COD crystals changes in a size-dependent manner.

The size of COD crystals may affect endocytosis. Small crystals can easily enter cells. The internalized COD crystals are then distributed in the cytoplasm and incorporated into lysosomes via vesicular transport. Intracellular lysosome contains a variety of acid hydrolases [50] that could

dissolve the internalized crystals into  $\text{Ca}^{2+}$  and  $\text{Ox}^{2-}$  ions for excretion [51]. At the same time, excessive levels of internalized crystals beyond the natural digestion capacity of cells aggravate cell injury [34]. Some of the COD crystals could pass through epithelial cells and be transferred to the interstitium via transcytosis, which further induces cell injury and inflammation, eventually leading to stone formation [52].

## 5. Conclusions

Five COD crystals of varying sizes were prepared and their injury ability toward Vero cells was comparatively studied. All of the COD crystals could decrease cell viability, increase cell apoptosis rate, and cause changes in biochemical parameters (LDH, SOD, ROS, HA, OPN, and  $\Delta\psi/m$ ) in a size-dependent manner. The cytotoxicity induced by COD was found to be size-dependent and follows the order  $50 \text{ nm} > 100 \text{ nm} > 600 \text{ nm} > 3 \mu\text{m} > 10 \mu\text{m}$ . Small crystals are more easily internalized by Vero cells compared to large crystals, which explains the difference in the severity of cell injury. The high cell toxicity induced by nano-COD crystals may be attributed to their greater active sites, higher surface energy, and larger surface area. Cell death rate was found to be positively related to the amount of internalized COD crystals. Cell toxicity induced by large COD crystals was weaker mainly due to their low contact probability and the decrease in total area of the  $\text{Ca}^{2+}$  ion-rich (100) face. Our study reveals the relationship between crystal size and renal epithelial cell injury, this will provide an insight into the underlying pathogenesis of nephrolithiasis.

## Acknowledgements:

This work was supported by National Natural Science Foundation of China (NO. 21371077).

## Notes and references

[1] Aggarwal K P, Narula S, Kakkar M, Tandon C. Nephrolithiasis: molecular mechanism of renal

- stone formation and the critical role played by modulators. *Biomed. Res. Int.*, 2013, 2013: 1-21.
- [2] Tsujihata M. Mechanism of calcium oxalate renal stone formation and renal tubular cell injury. *Int. J. Urol.*, 2008, 15(2): 115-120.
- [3] Kok D J, Khan S R. Calcium oxalate nephrolithiasis, a free or fixed particle disease. *Kidney Int.*, 1994, 46(3): 847-854.
- [4] Chaiyarit S, Thongboonkerd V. Changes in mitochondrial proteome of renal tubular cells induced by calcium oxalate monohydrate crystal adhesion and internalization are related to mitochondrial dysfunction. *J. Proteome Res.*, 2012, 11(6): 3269-3280.
- [5] Fishman A I, Green D, Lynch A, Choudhury M, Eshghi M, Konno S. Preventive effect of specific antioxidant on oxidative renal cell injury associated with renal crystal formation. *Urology*, 2013, 82(2): 489.e481-487.
- [6] An Z, Lee S, Oppenheimer H, Wesson J A, Ward M D. Attachment of calcium oxalate monohydrate crystals on patterned surfaces of proteins and lipid bilayers. *J. Am. Chem. Soc.*, 2010, 132(38): 13188-13190.
- [7] Wang B, Wu B, Liu J, Yao W, Xia D, Li L, Chen Z, Ye Z, Yu X. Analysis of altered microRNA expression profiles in proximal renal tubular cells in response to calcium oxalate monohydrate crystal adhesion: implications for kidney stone disease. *PloS one*, 2014, 9(7): e101306.
- [8] Peerapen P, Thongboonkerd V. Effects of calcium oxalate monohydrate crystals on expression and function of tight junction of renal tubular epithelial cells. *Lab. Invest.*, 2011, 91(1): 97-105.
- [9] Khan A, Byer K, Khan S R. Exposure of Madin-Darby canine kidney (MDCK) cells to oxalate and calcium oxalate crystals activates nicotinamide adenine dinucleotide phosphate (NADPH)-oxidase. *Urology*, 2014, 83(2): 510.e511-517.
- [10] Martin X, Smith L H, Werness P G. Calcium oxalate dihydrate formation in urine. *Kidney Int.*, 1984, 25(6): 948-952.

- [11] Semangoen T, Sinchaikul S, Chen S-T, Thongboonkerd V. Altered proteins in MDCK renal tubular cells in response to calcium oxalate dihydrate crystal adhesion: A proteomics approach. *J. Proteome Res.*, 2008, 7(7): 2889-2896.
- [12] Yuen J W M, Gohel M-D I, Poon N-w, Shum D K Y, Tam P-c, Au D W T. The initial and subsequent inflammatory events during calcium oxalate lithiasis. *Clin. Chim. Acta*, 2010, 411(15-16): 1018-1026.
- [13] Mueller W E G, Schroeder H C, Schlossmacher U, Grebenjuk V A, Ushijima H, Wang X. Induction of carbonic anhydrase in SaOS-2 cells, exposed to bicarbonate and consequences for calcium phosphate crystal formation. *Biomaterials*, 2013, 34(34): 8671-8680.
- [14] Ali M R K, Panikkanvalappil S R, El-Sayed M A. Enhancing the efficiency of gold nanoparticles treatment of cancer by increasing their rate of endocytosis and cell accumulation using rifampicin. *J. Am. Chem. Soc.*, 2014, 136(12): 4464-4467.
- [15] Lesniak A, Salvati A, Santos-Martinez M J, Radomski M W, Dawson K A, Åberg C. Nanoparticle adhesion to the cell membrane and its effect on nanoparticle uptake efficiency. *J. Am. Chem. Soc.*, 2013, 135: 1438-1444.
- [16] Karlsson H L, Gustafsson J, Cronholm P, Moller L. Size-dependent toxicity of metal oxide particles-A comparison between nano- and micrometer size. *Toxicol. Lett.*, 2009, 188(2): 112-118.
- [17] Yang X, Liu J, He H, Zhou L, Gong C, Wang X, Yang L, Yuan J, Huang H, He L, Zhang B, Zhuang Z. SiO<sub>2</sub> nanoparticles induce cytotoxicity and protein expression alteration in HaCaT cells. *Part. Fibre Toxicol.*, 2010, 7: 1.
- [18] Duan C-Y, Xia Z-Y, Zhang G-N, Gui B-S, Xue J-F, Ouyang J-M. Changes in urinary nanocrystallites in calcium oxalate stone formers before and after potassium citrate intake. *Int. J. Nanomed.*, 2013, 8: 909-918.

- [19] Verdesca S, Fogazzi G B, Garigali G, Messa P, Daudon M. Crystalluria: prevalence, different types of crystals and the role of infrared spectroscopy. *Clin. Chem. Lab. Med.*, 2011, 49(3): 515-520.
- [20] Daudon M, Hennequin C, Boujelben G, Lacour B, Jungers P. Serial crystalluria determination and the risk of recurrence in calcium stone formers. *Kidney Int.*, 2005, 67(5): 1934-1943.
- [21] Robertson W G, Peacock M, Nordin B E C. Calcium crystalluria in recurrent renal-stone formers. *The Lancet*, 1969, 294(7610): 21-24.
- [22] He J-Y, Deng S-P, Ouyang J-M. Morphology, size distribution, aggregation, and crystal phase of nanocrystallites in urines of healthy persons and lithogenic patients. *IEEE Trans. Nanobiosci.*, 2010, 9(2): 156-163.
- [23] Marickar Y M F, Lekshmi P R, Varma L, Koshy P. Elemental distribution analysis of urinary crystals. *Urol. Res.*, 2009, 37(5): 277-282.
- [24] Tunik L, Fueredi-Milhofer H, Garti N. Adsorption of sodium diisooctyl sulfosuccinate onto calcium oxalate crystals. *Langmuir*, 1998, 14(12): 3351-3355.
- [25] Thongboonkerd V, Semangoen T, Chutipongtanate S. Factors determining types and morphologies of calcium oxalate crystals: Molar concentrations, buffering, pH, stirring and temperature. *Clin. Chim. Acta*, 2006, 367(1-2): 120-131.
- [26] Wulff G. On the question of speed of growth and dissolution of crystal surfaces. *Z. Krystallogr. Mineral.*, 1901, 34: 449-530.
- [27] Mettela G, Boya R, Singh D, Kumar G P, Kulkarni G. Highly tapered pentagonal bipyramidal Au microcrystals with high index faceted corrugation: Synthesis and optical properties. *Sci. Rep.*, 2013, 3: 1-8.
- [28] Vanachayangkul P, Byer K, Khan S, Butterweck V. An aqueous extract of Ammi visnaga fruits and its constituents khellin and visnagin prevent cell damage caused by oxalate in renal

- epithelial cells. *Phytomedicine*, 2010, 17(8-9): 653-658.
- [29] Khan S R. Hyperoxaluria-induced oxidative stress and antioxidants for renal protection. *Urol. Res.*, 2005, 33(5): 349-357.
- [30] Verkoelen C F. Crystal retention in renal stone disease: A crucial role for the glycosaminoglycan hyaluronan?. *J. Am. Soc. Nephrol.*, 2006, 17(6): 1673-1687.
- [31] Grohe B, O'Young J, Ionescu D A, Lajoie G, Rogers K A, Karttunen M, Goldberg H A, Hunter G K. Control of calcium oxalate crystal growth by face-specific adsorption of an osteopontin phosphopeptide. *J. Am. Chem. Soc.*, 2007, 129(48): 14946-14951.
- [32] Salvioli S, Ardizzoni A, Franceschi C, Cossarizza A. JC-1, but not DiOC6(3) or rhodamine 123, is a reliable fluorescent probe to assess  $\Delta\Psi$  changes in intact cells: implications for studies on mitochondrial functionality during apoptosis. *FEBS Lett*, 1997, 411(1): 77-82.
- [33] Sheng X X, Ward M D, Wesson J A. Crystal surface adhesion explains the pathological activity of calcium oxalate hydrates in kidney stone formation. *J. Am. Soc. Nephrol.*, 2005, 16(7): 1904-1908.
- [34] Hovda K E, Guo C, Austin R, McMartin K E. Renal toxicity of ethylene glycol results from internalization of calcium oxalate crystals by proximal tubule cells. *Toxicol. Lett.*, 2010, 192(3): 365-372.
- [35] Mersmann A. Crystallization and precipitation. *Chem. Eng. Process.*, 1999, 38(4-6): 345-353.
- [36] Marangella M, Daniele P G, Ronzani M, Sonuga S, Linari F. Urine saturation with calcium salts in normal subjects and idiopathic calcium stone formers estimated by an improved computer model system. *Urol. Res.* 1985, 13: 189-193.
- [37] Shapur N K, Uvarov V, Popov I, Katz R, Gofrit O N, Landau E H, Pode D, Duvdevani M. Crystallite size-is it a new predictor for renal stone burden? *Urology*, 2012, 80(5): 980-985.
- [38] Meng H, Xia T, George S, Nel A E. A predictive toxicological paradigm for the safety

- assessment of nanomaterials. *ACS Nano*, 2009, 3(7): 1620-1627.
- [39] Nel A, Xia T, Madler L, Li N. Toxic potential of materials at the nanolevel. *Science*, 2006, 311(5761): 622-627.
- [40] Li N, Sioutas C, Cho A, Schmitz D, Misra C, Sempf J, Wang M Y, Oberley T, Froines J, Nel A. Ultrafine particulate pollutants induce oxidative stress and mitochondrial damage. *Environ. Health Perspect*, 2003, 111(4): 455-460.
- [41] Hu Q, Cai Y, Shi Z, Yan W, Tang R. Inhibition of proliferation of osteosarcoma by nano calcium phosphates: potential hard tissue repair after tumor extraction. *Front. Mater. Sci. China*, 2007, 1(1): 30-34.
- [42] Li Y, Sun L, Jin M, Du Z, Liu X, Guo C, Li Y, Huang P, Sun Z. Size-dependent cytotoxicity of amorphous silica nanoparticles in human hepatoma HepG2 cells. *Toxicol. in Vitro*, 2011, 25(7): 1343-1352.
- [43] Lieske J C, Toback F G, Deganello S. Face-selective adhesion of calcium oxalate dihydrate crystals to renal epithelial cells. *Calcif. Tissue Int.*, 1996, 58(3): 195-200.
- [44] Riese R J, Mandel N S, Wiessner J H, Mandel G S, Becker C G, Kleinman J G. Cell polarity and calcium oxalate crystal adherence to cultured collecting duct cells. *Am. J. Physiol.*, 1992, 262(2 Pt 2): F177-184.
- [45] Lieske J C, Toback F G. Regulation of renal epithelial cell endocytosis of calcium oxalate monohydrate crystals. *Am. J. Physiol.*, 1993, 264(5 Pt 2): F800-807.
- [46] Hauck T S, Ghazani A A, Chan W C W. Assessing the effect of surface chemistry on gold nanorod uptake, toxicity, and gene expression in mammalian cells. *Small*, 2008, 4(1): 153-159.
- [47] Zhao F, Zhao Y, Liu Y, Chang X, Chen C, Zhao Y. Cellular uptake, intracellular trafficking, and cytotoxicity of nanomaterials. *Small*, 2011, 7(10): 1322-1337.
- [48] Umekawa T, Tsuji H, Uemura H, Khan S R. Superoxide from NADPH oxidase as second

- messenger for the expression of osteopontin and monocyte chemoattractant protein-1 in renal epithelial cells exposed to calcium oxalate crystals. *BJU Int.*, 2009, 104(1): 115-120.
- [49] Wiessner J H, Hasegawa A T, Hung L Y, Mandel G S, Mandel N S. Mechanisms of calcium oxalate crystal attachment to injured renal collecting duct cells. *Kidney Int.*, 2001, 59(2): 637-644.
- [50] Watts C. The endosome-lysosome pathway and information generation in the immune system. *Biochim. Biophys. Acta*, 2012, 1824(1): 14-21.
- [51] Grover P K, Thurgood L A, Fleming D E, van Bronswijk W, Wang T, Ryall R L. Intracrystalline urinary proteins facilitate degradation and dissolution of calcium oxalate crystals in cultured renal cells. *Am. J. Physiol. Renal Physiol.*, 2008, 294(2): F355-F361.
- [52] Sayer J A, Carr G, Simmons N L. Nephrocalcinosis: molecular insights into calcium precipitation within the kidney. *Clin. Sci.*, 2004, 106(6): 549-561.

## Captions

Table 1. Contact probability between Vero cells and varying sizes of COD crystals under fixed crystal concentration of 200  $\mu\text{g}/\text{mL}$ .

Fig. 1. SEM images of COD crystals of varying sizes.(a) 50 nm; (b) 100 nm;(c) 600nm; (d) 3  $\mu\text{m}$ ; (e) 10  $\mu\text{m}$ . Scale bars: (a-c) 200 nm; (d) 1  $\mu\text{m}$ ; (e) 5  $\mu\text{m}$ .

Fig. 2. Schematic representation of morphology and crystal face variation of COD crystals with crystal size increase. (a) Nano-scale, spherical; (b) submicron, thick tetragonal bipyramid; (c) micron, thin tetragonal bipyramid.

Fig. 3. Change in cell viability (a), LDH release amount (b), and SOD activity (c) of Vero cells after exposure to varying sizes of COD crystals for 6 h. Crystal concentration: 200  $\mu\text{g}/\text{mL}$ .

Fig. 4. Intracellular ROS level of Vero cells after exposure to varying sizes of COD crystals for 6 h. (A) histogram of intracellular ROS; (b) quantitative results of intracellular ROS. Crystal size was marked above and below the box.

Fig. 5. Hyaluronan expression in Vero cells after exposure to varying sizes of COD crystals for 6 h. (A) Laser scanning confocal microscope images; (B) Quantitative results of expressed HA. Bars: 20  $\mu\text{m}$ .

Fig. 6. OPN expression in Vero cells after treatment with varying sizes of COD crystals for 6 h detected by laser scanning confocal microscope. Scale bars: 20  $\mu\text{m}$

Fig. 7. Effect of varying sizes of COD crystals on mitochondrial membrane potential ( $\Delta\psi_m$ ) in Vero cells. (a) Dot plot of  $\Delta\psi_m$  after incubation with varying sizes of COD for 6 h; (b) quantitative histogram of  $\Delta\psi_m$ ; (c) quantitative histogram of  $\Delta\psi_m$  after treatment with 50 nm and 10  $\mu\text{m}$  COD crystals under different treatment times.

Fig. 8. Cellular apoptosis of Vero cells after exposure to varying sizes of COD crystals for 6 h. (a) Dot plots of cellular apoptosis. Quadrants Q1, Q2, Q3, and Q4 denote the ratio of necrotic cells, late-stage apoptotic cells, normal cells, and early-stage apoptotic cells, respectively. (b) Quantitative results of cellular apoptosis.

Fig. 9. SEM images of COD crystals after exposure to varying sizes of COD for 6 h. (a) 50 nm; (b) 100 nm; (c) 600 nm; (d) 3  $\mu\text{m}$ ; (e) 10  $\mu\text{m}$ . Crystal concentration: 200  $\mu\text{g/mL}$ . Adhesion time: 6 h. Scale bars: (a, b) 2  $\mu\text{m}$ ; (c,d) 5  $\mu\text{m}$ ; (e) 10  $\mu\text{m}$ .

Fig. 10. SEM images of 10  $\mu\text{m}$  COD crystals that adhered to Vero cells (a,b). The cells with adhered crystals were seriously injured; the cells without adhered crystals were minimally injured (c,d). Scale bars: 5  $\mu\text{m}$ .

Fig. 11. Quantitative analysis of varying sizes of COD internalized by Vero cells (a) and the correlation between COD internalization and cell death rate (b).

Fig. 12. A proposed schematic illustration of cellular and molecular mechanism of Vero cell injury after exposure to varying sizes of COD crystals. (a) Mechanism of oxidative damage induced by exposure to COD crystals; (b) Cellular fate of internalized COD crystals.

Table 1. Contact probability between Vero cells and varying sizes of COD crystals under fixed crystal concentration of 200  $\mu\text{g/mL}$ .

Crystal size $d/\text{nm}$	50 nm	100 nm	600nm	3 $\mu\text{m}$	10 $\mu\text{m}$
Mass of a single COD crystal / $\mu\text{g}$ <sup>*1</sup>	$1.27 \times 10^{-10}$	$1.02 \times 10^{-9}$	$2.19 \times 10^{-7}$	$2.74 \times 10^{-5}$	$1.02 \times 10^{-3}$
Relative ratio of crystal mass	1	8.0	1 724	$2.16 \times 10^6$	$8.03 \times 10^6$
Number of adhered COD crystals ( $N_{\text{crystal}}$ ) / <sup>*2</sup>	$4.10 \times 10^{11}$	$5.11 \times 10^{10}$	$2.38 \times 10^8$	$1.90 \times 10^6$	$5.11 \times 10^4$
Number of adhered COD crystals on a cell / <sup>*3</sup>	$1.29 \times 10^6$	$1.61 \times 10^5$	$7.48 \times 10^2$	5.97	0.16

<sup>\*1</sup>: The density of COD crystal:  $\rho_{(\text{COD})} = 1.94 \text{ g/cm}^3$ .

<sup>\*2</sup>: The mean diameter of Vero cell is about 20  $\mu\text{m}$  (Fig. 10). If a cell is regarded as a sphere, the area of each cell is approximate  $3.14 \times 10^{-4} \text{ mm}^2$ . If the cell is closely connected, an area of  $10\text{mm} \times 10\text{mm}$  contains about  $3.18 \times 10^5$  cells ( $N_{\text{cell}}$ ). Since the hole diameter ( $d$ ) of 12-well cell culture plate used in this experiment is 22.1 mm, the area of each hole is  $383.6 \text{ mm}^2$ ; when 200  $\mu\text{g}$  COD crystal was added to each hole, the mass of COD crystals ( $W$ ) in an area of  $10\text{mm} \times 10\text{mm}$  was  $(200\mu\text{g}/383.6\text{mm}^2) \times 100\text{mm}^2 = 52.14 \mu\text{g}$ . Taking 50 nm COD crystal as an example, the number of adhered crystals in this area ( $N_{\text{crystal}}$ ) was:  $52.14 \mu\text{g}/(1.27 \times 10^{-10}) = 4.10 \times 10^{11}$ .

<sup>\*3</sup>:  $N_{\text{crystal}}/N_{\text{cell}} = 4.10 \times 10^{11}/3.18 \times 10^5 = 1.29 \times 10^6$ .

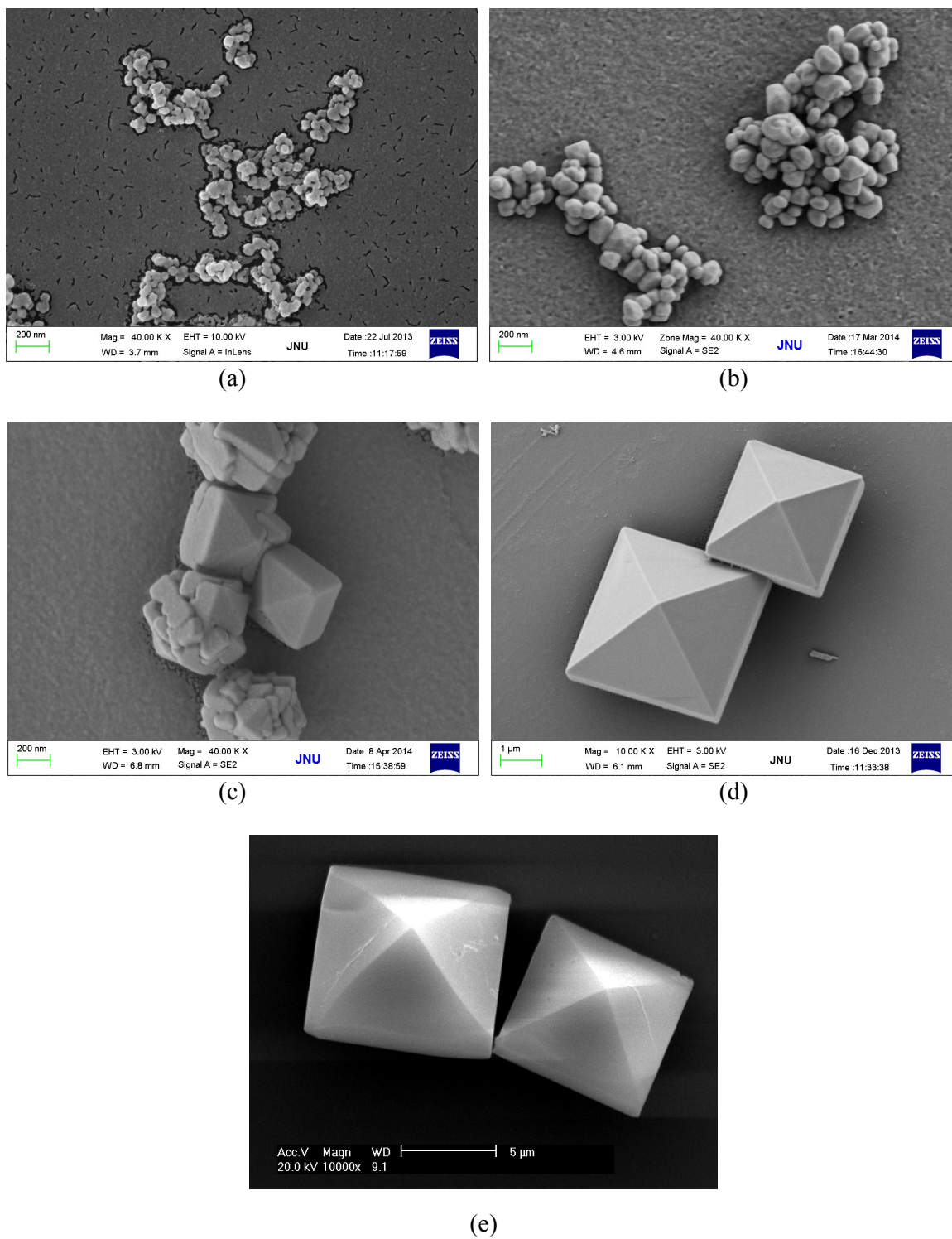


Fig. 1.

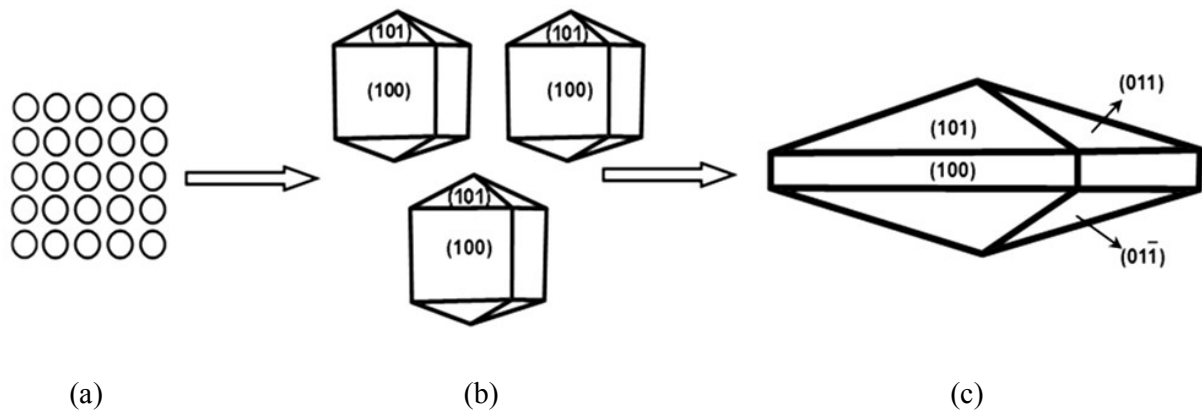


Fig. 2.

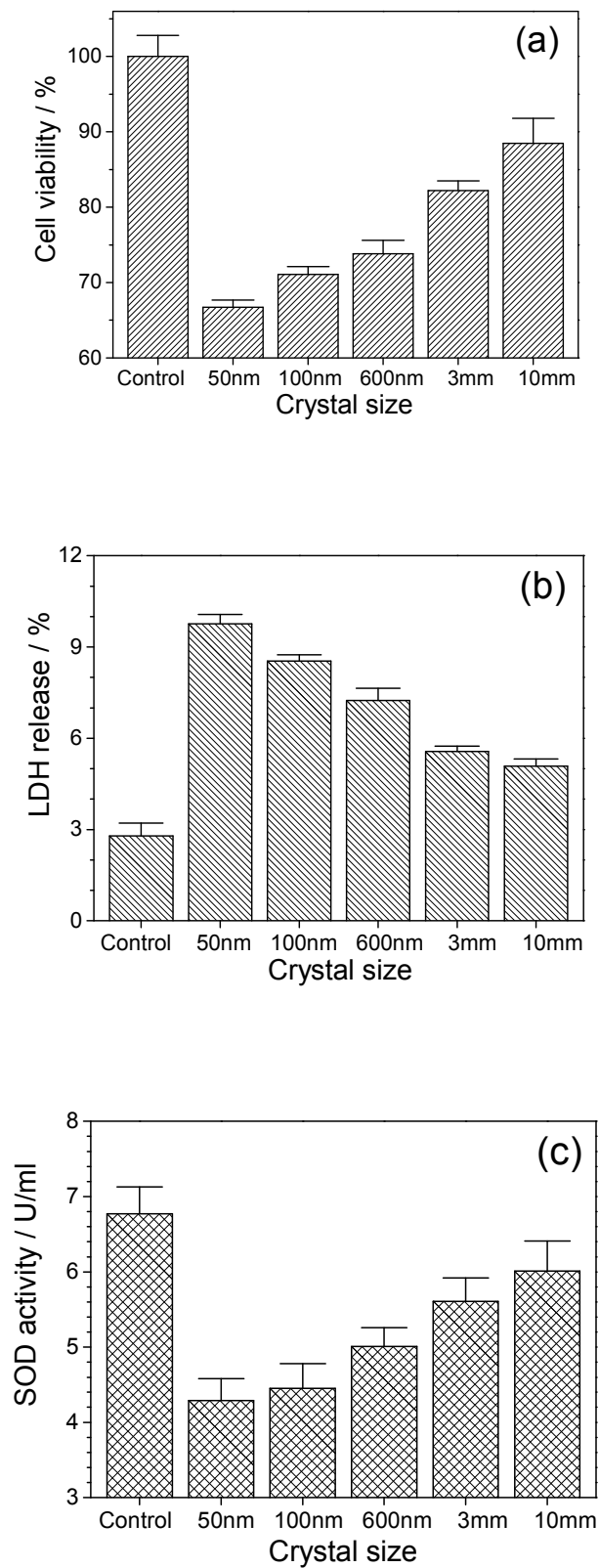


Fig. 3.

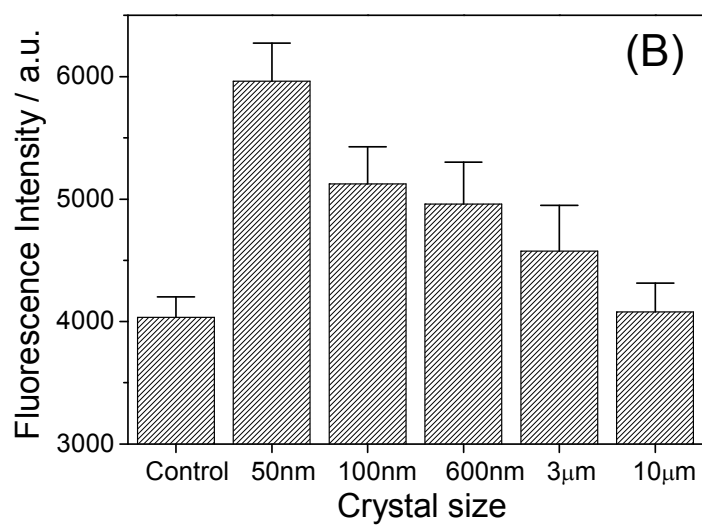
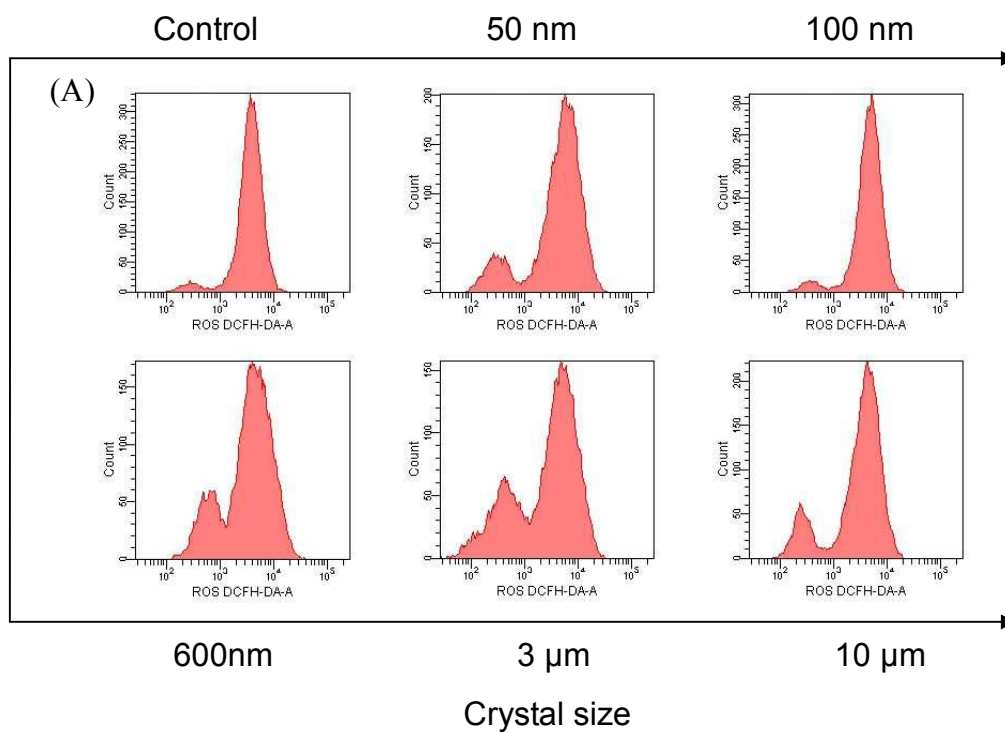


Fig. 4.

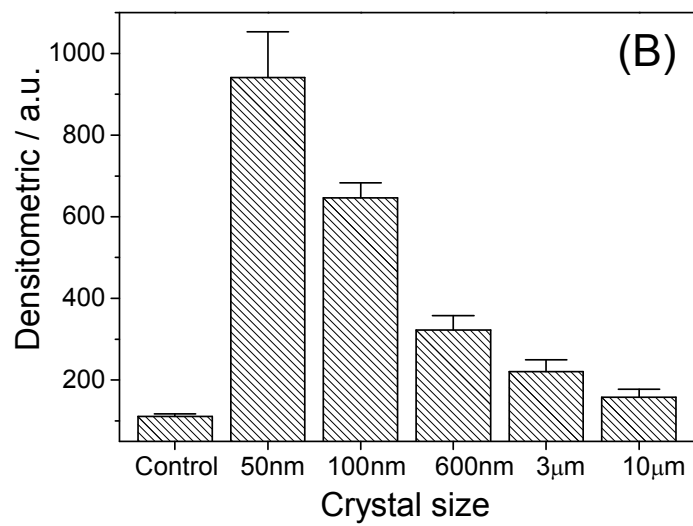
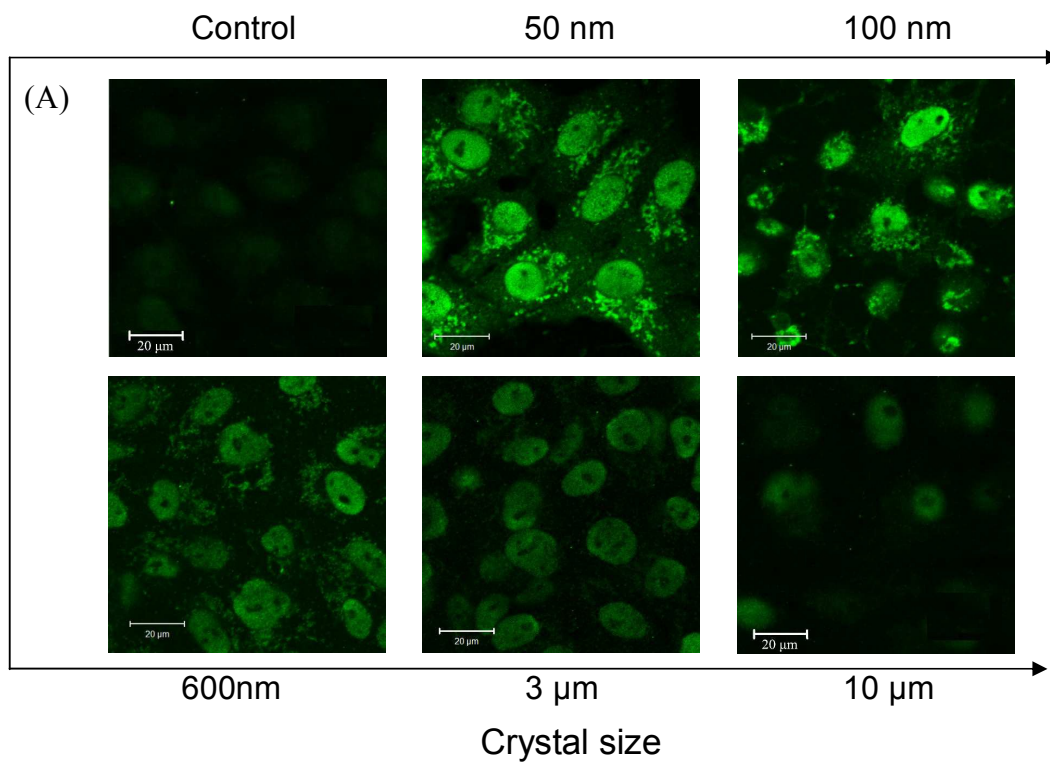


Fig. 5.

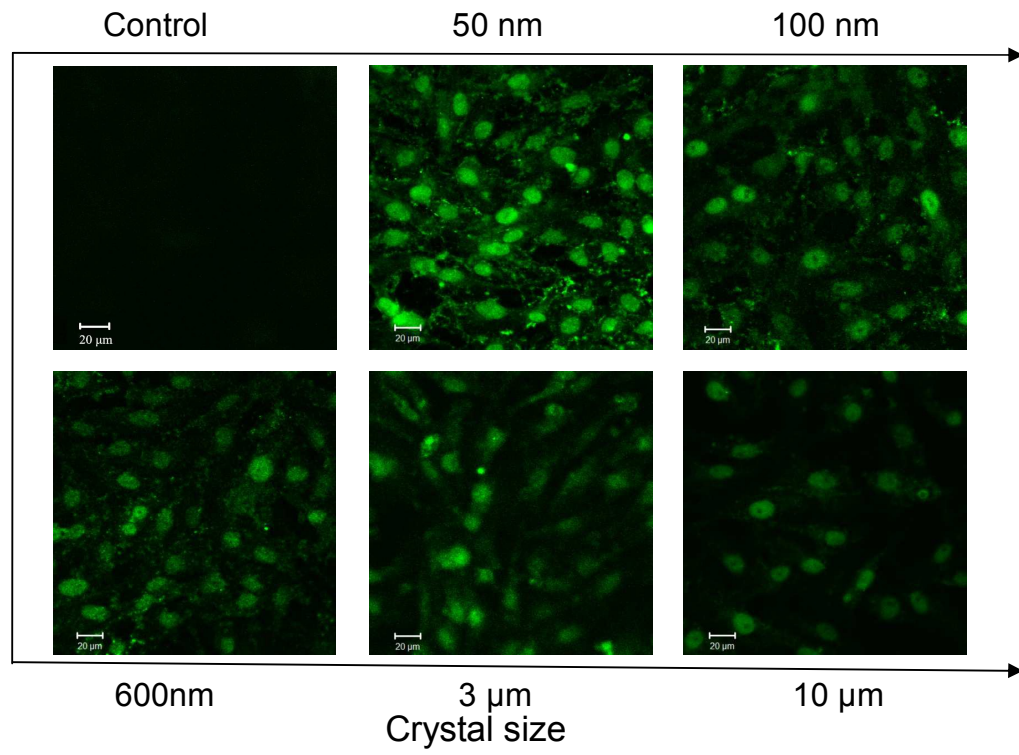


Fig. 6.

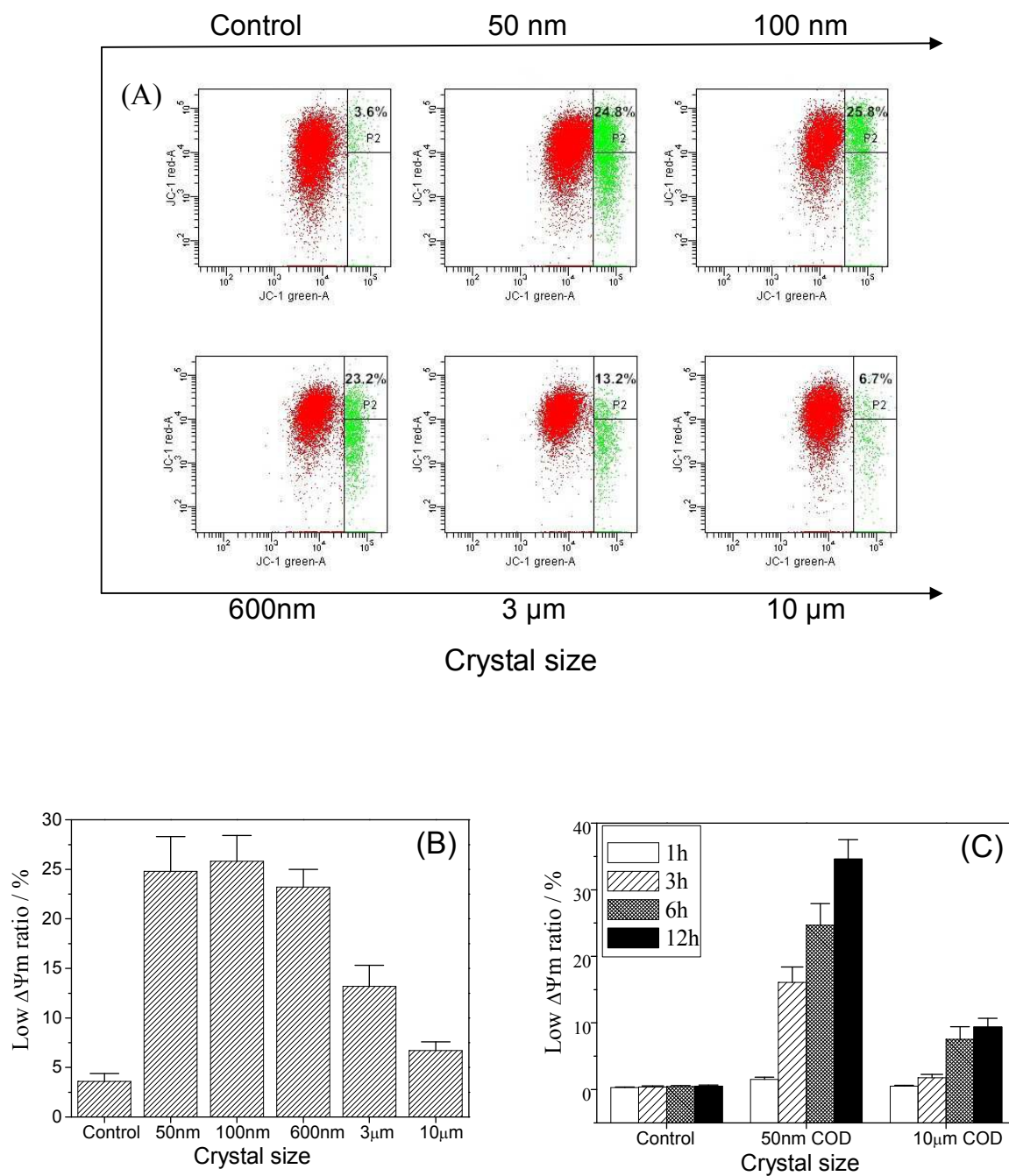


Fig. 7.

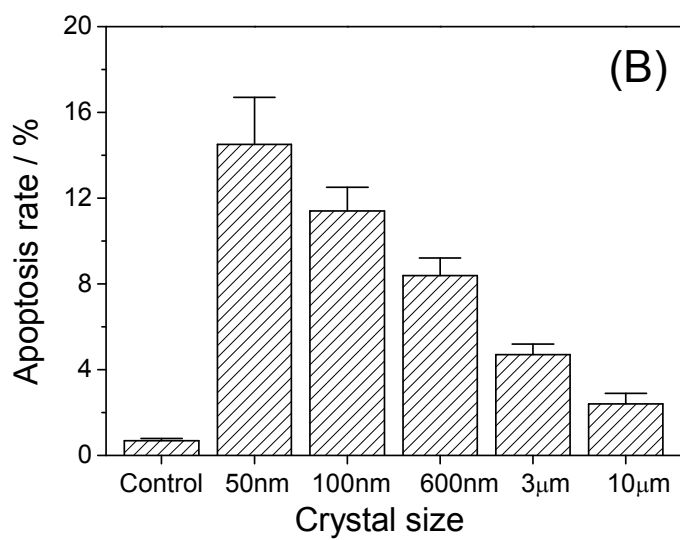
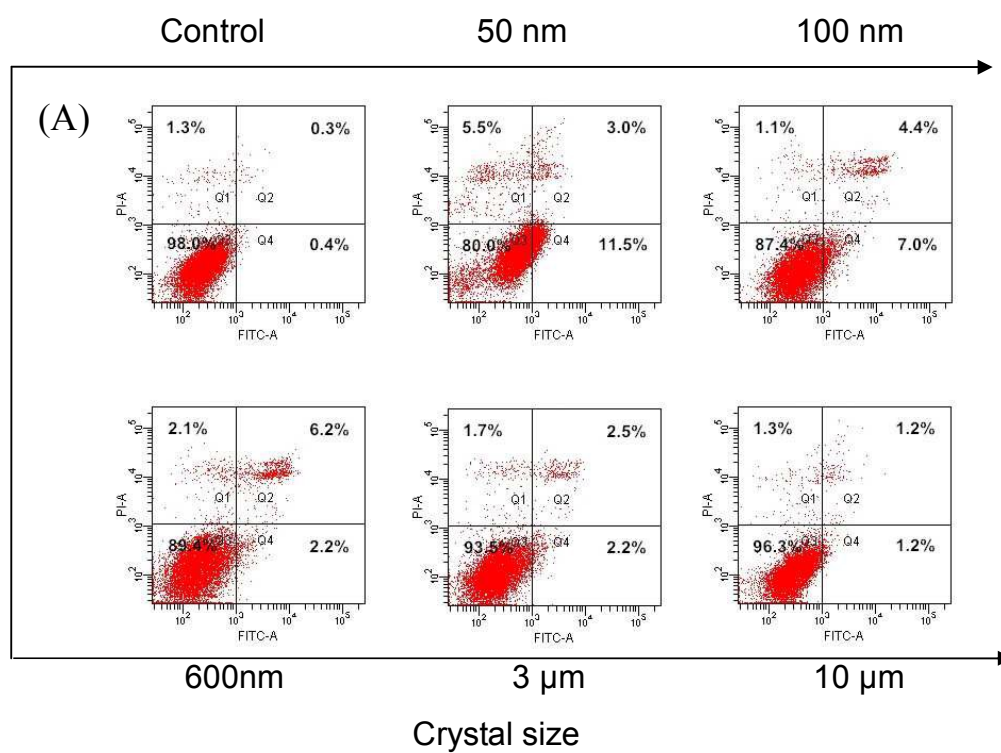


Fig. 8.

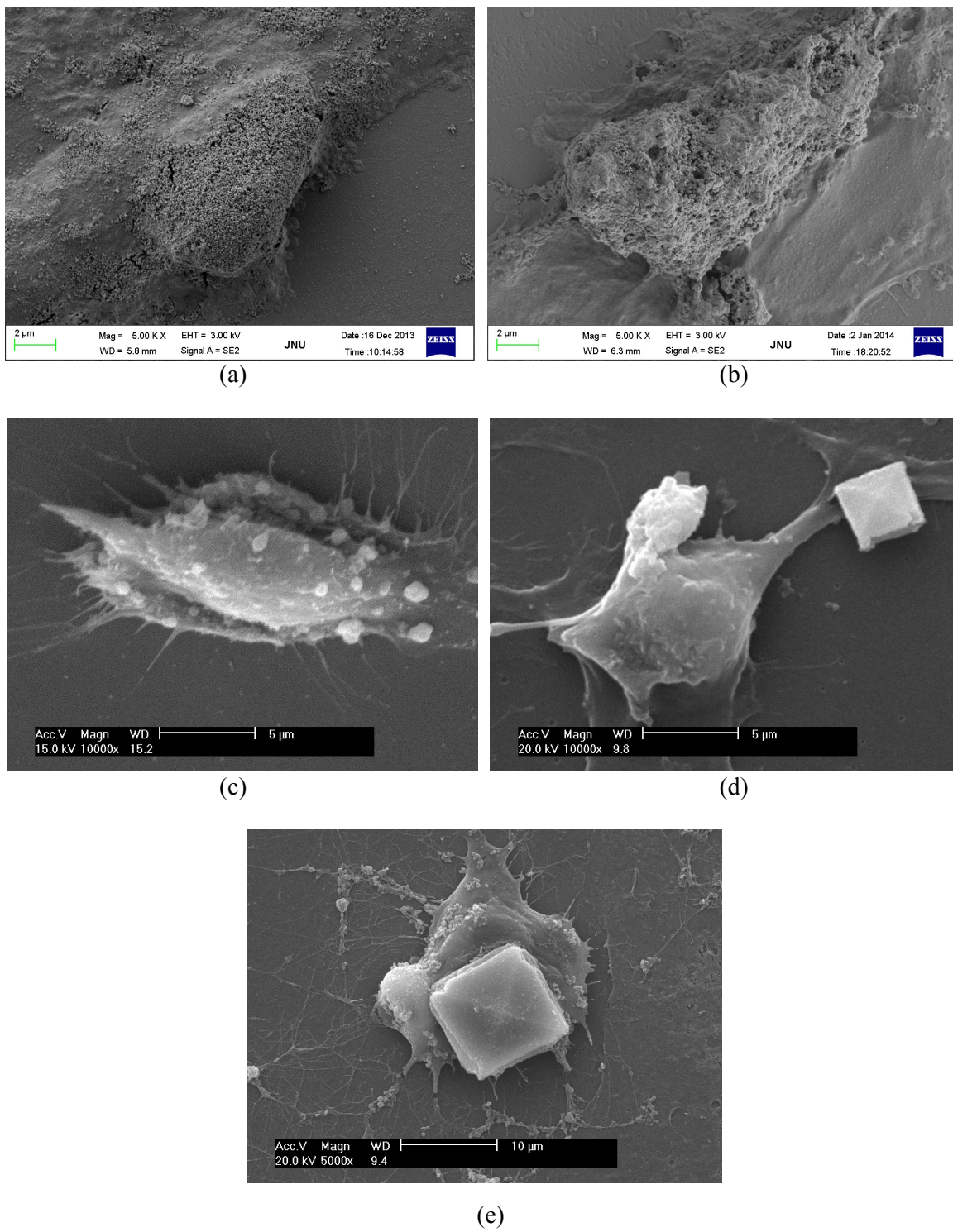


Fig. 9.

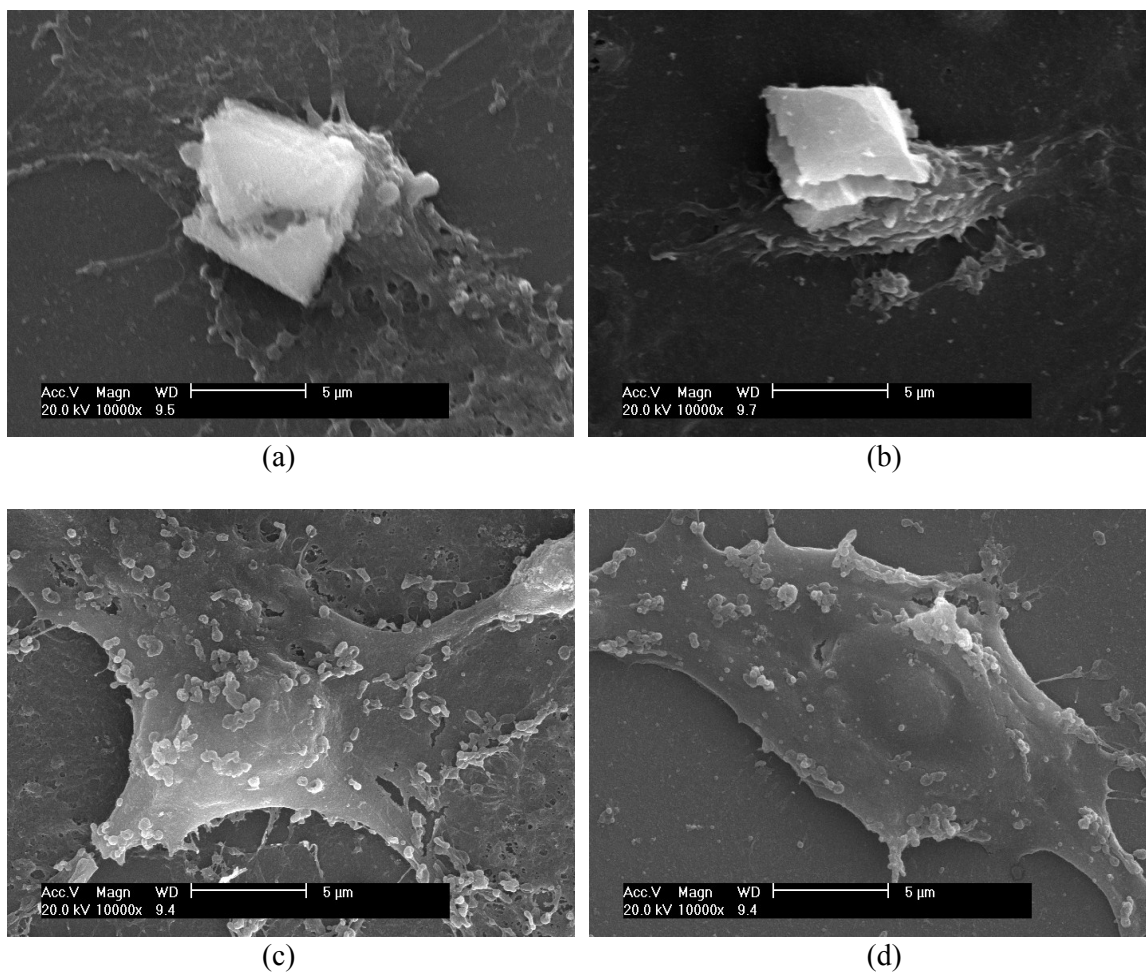


Fig. 10.

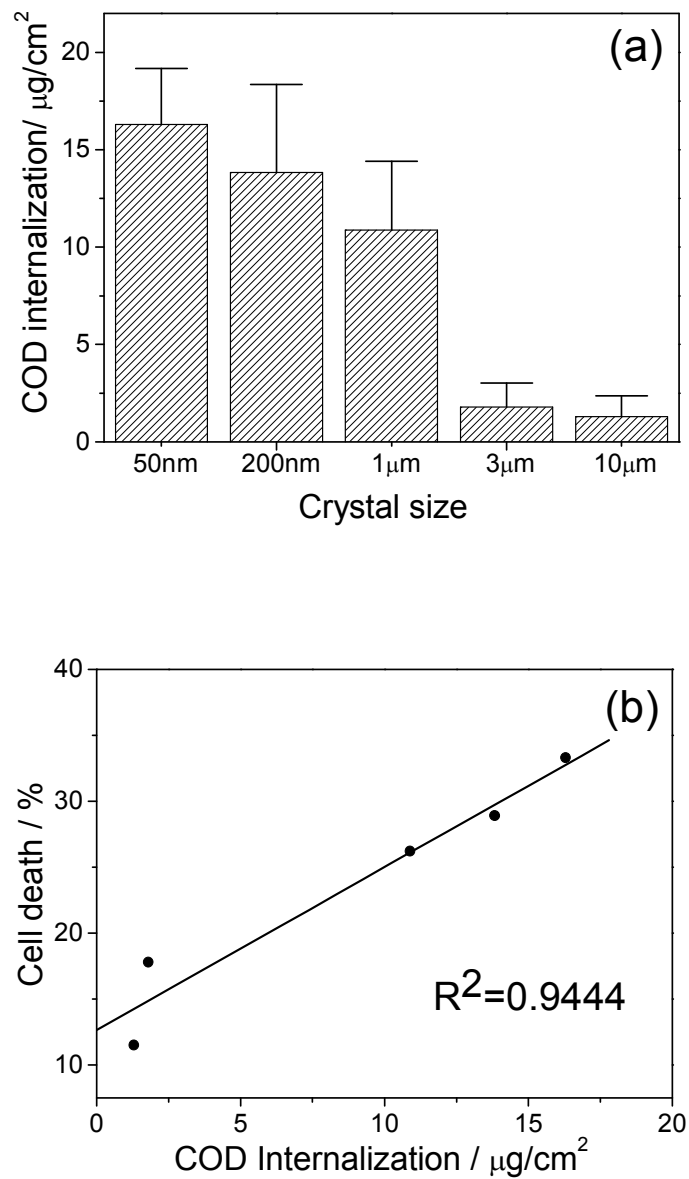


Fig. 11.

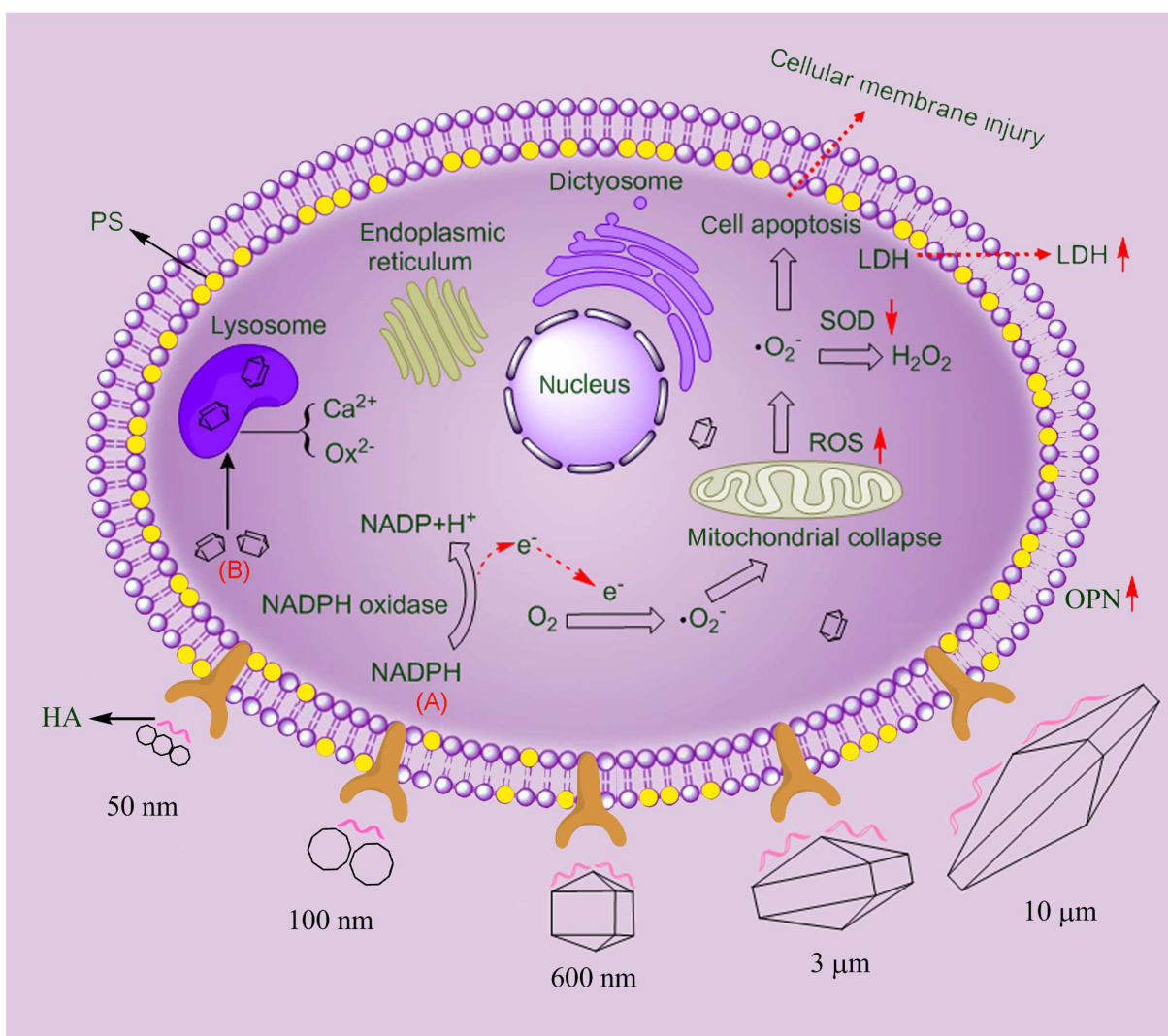


Fig. 12.

